International Scientific Conference 20 UNITECH 26

INTERNATIONAL SCIENTIFIC CONFERENCE
19-21 November 2026
GABROVO

WEIGHT-ORIENTED DESIGN OF SQUARE HOLLOW SECTION BEAMS IN THREE-POINT BENDING: OPENING AND WALL THICKNESS VARIANTS COMPARED BY NONLINEAR FINITE ELEMENT ANALYSIS

Gürkan İRSEL[1]

[1]*Trakya University, Faculty of Engineering, Department of Mechanical Engineering, Edirne 22100, Türkiye*

**Corresponding author: gurkanirsel@trakya.edu.tr*

Abstract

Cutting openings near the neutral axis is a common way to reduce the mass of bending members. Openings lower the stiffness, so the wall must be thickened; the net saving is unclear. A 60 × 60 × 6 mm S355 square hollow section without openings (reference, R6) is compared in three-point bending with twelve profiles whose side walls carry 16 openings along the neutral axis (circular or square, equal-sized or graded; 6, 7 and 8 mm walls). Bending to 10 mm displacement was solved with ANSYS 2020 R1. By interpolation over the three thicknesses, the equivalent wall thickness at which a perforated profile equals the reference in initial stiffness, force at 8 mm and energy was found; computation times are given. At 6 mm the perforated profiles are 5.1–6.1 % lighter than the reference; their initial stiffness is 8.2–11.6 % lower, while the force they carry at 8 mm is at most 2.1 % lower. Equal force at 8 mm requires a 6.0–6.1 mm wall (mass 4.4–5.1 % lower); equal initial stiffness requires 6.7–7.0 mm (mass 3.0–6.2 % higher). Perforation saves 4–5 % of mass if force or energy at large displacement governs, but adds 3–6 % if stiffness governs.

Keywords: Weight-Oriented Design; Square Hollow Section; Perforated Wall; Nonlinear Bending; Finite Element Analysis

1. INTRODUCTION

Openings in the walls of hollow sections reduce material consumption and allow connections and services to pass, but they also alter load transfer and local stresses; mass reduction therefore has to be judged together with stiffness and the force carried at prescribed displacements. Perforated steel beams have mostly been studied as open sections: Tsavdaridis and D'Mello examined the influence of web-opening geometry on web-post buckling and strength [1], Ellobody the interaction of buckling modes in castellated beams [2], Sweedan and El-Sawy the elastic local buckling of perforated webs [3], Sonck and Belis the lateral–torsional buckling resistance of cellular beams [4], and Shanmugam et al. the finite element modelling of plate girders with web openings [5].

For closed sections, Vadivelu et al. investigated the flexure of perforated cold-formed rectangular hollow sections experimentally and numerically [6], Cosgun and Akcan square hollow sections with oval openings under eccentric compression [7], Chen et al. the design of perforated ferritic stainless-steel rectangular hollow sections [8], Prabowo et al. and Prabowo stainless-steel sections with a single web opening at elevated temperatures [9, 10], Saoula et al. the lateral–torsional buckling of such sections [11], and Lifsey et al. hollow-flange beams with circular web openings [12]. These studies concern cold-formed or stainless-steel sections, mostly with a single

This is an open access article licensed under Creative Commons Attribution 4.0 International
Print ISSN: 1313-230X, Online ISSN: 3033-1404

opening or at elevated temperature, and report the capacity or buckling of the perforated section. In machine design, finite element analysis is used to check and lighten structures, for example in a CAD/CAE and structural optimisation procedure demonstrated on a tractor-mounted telescopic boom crane [13] and in the stress analysis of the transmission gears of a rotary drum mower [14].

A search of the OpenAlex database in October 2026 (ten queries, 206 records, 75 screened by title and abstract) identified the studies [6, 8–12]; six further queries on perforated square and rectangular hollow sections and perforated tubes added Ridley-Ellis et al., who tested rectangular hollow sections with circular side-wall openings in three- and four-point bending and extended the work with a finite element study of the opening diameter [15], Dundar and Nuraliyev, who studied the local buckling of perforated square sections with non-uniform wall thickness under axial compression [16], and Gajewski et al., who optimised thin-walled beams with openings for stiffness and weight, the procedure being presented for open sections [17]. In the records examined, no study expresses the effect of side-wall perforation of a square hollow section as the wall thickness at which it matches a solid-wall reference in stiffness, force and energy in a nonlinear elastic–plastic model. This is the question addressed here: a 60 × 60 × 6 mm S355 section is compared with twelve perforated variants that are generated parametrically from the opening shape, size, arrangement and wall thickness, using the material model of an earlier study [18].

2. MODELS AND METHODS

2.1 Geometry

All sections are 60 × 60 mm and 500 mm long, with outer and inner corner radii 2t and t (t = wall thickness). The reference R6 has no openings and t = 6 mm; the perforated sections have t = 6, 7 and 8 mm (7 mm is not a standard size and serves to examine the thickness dependence and the interpolation). The span is 420 mm; the rollers have a diameter of 30 mm and a length of 100 mm, and the supports act on 80 × 106 × 4 mm plates under the profile ends (Fig. 1).

Openings are placed only in the two side walls, at the neutral-axis height, in the regions 80–220 mm and 280–420 mm from one end; the end zones and the loading zone from 220 to 280 mm are intact. Each wall has eight openings (16 in total), aligned in the two walls and symmetric about midspan. The shapes are circular (C) and square with 3 mm corner radii (K); the layouts are uniform (U, d = 22 mm, pitch 35 mm) and graded (G, d = 26, 22, 18, 14 mm from the supports towards the load at t = 6 and 7 mm, and 24, 22, 18, 14 mm at t = 8 mm, because the 26 mm opening does not fit into the 28 mm flat wall of the 8 mm section). The square side length is chosen so that the area equals that of the circle before corner rounding; the rounding reduces the area of the square openings by 1.4–5.1 % and makes the square variants 0.1 % heavier than the circular ones, so that the shape comparison is not exactly at equal area. Positions and sizes are given in Table 1 and Fig. 2. Models are labelled Pt_S_L (thickness, shape C or K, layout U or G). Profile masses are obtained from the volume of the CAD solid of the profile and a density of 7,850 kg/m³; plates and rollers are not included.

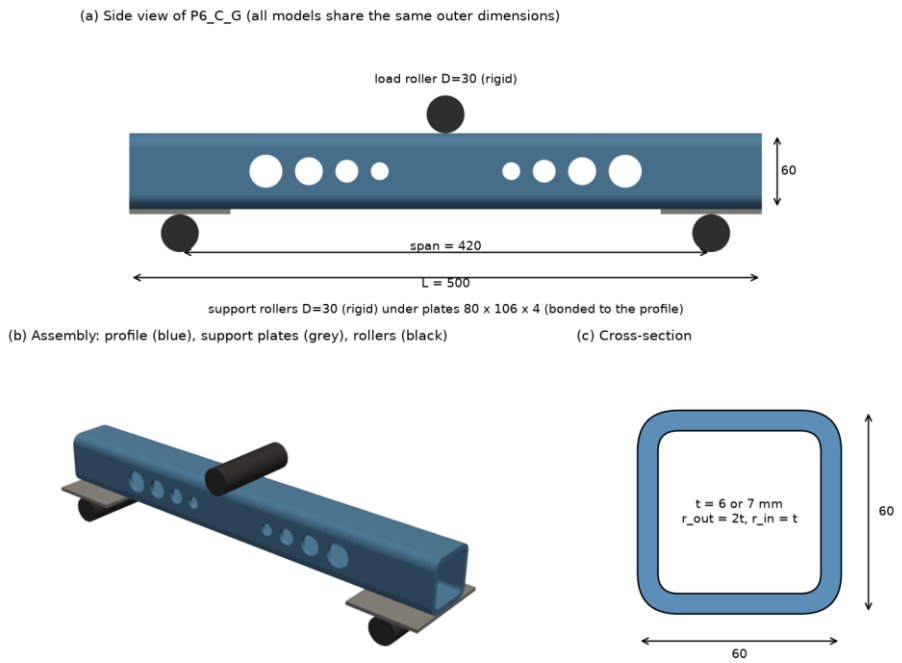


Fig. 1. *(a) side view with dimensions, (b) assembly (profile, plates, rollers), (c) cross-section (60 × 60 mm, wall t, radii 2t and t); the example is P6_C_G.*

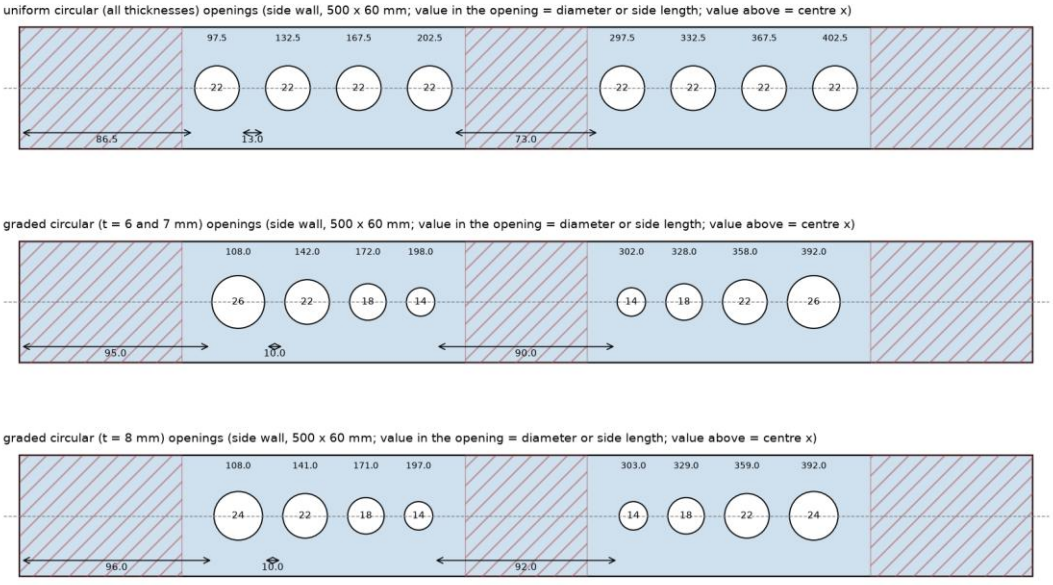


Fig. 2. *opening layout on the side wall (500 × 60 mm) for the uniform layout and the graded layouts (t = 6, 7 mm and t = 8 mm), shown with circular openings; hatched zones are free of openings. The square openings have the same centres and the sizes of Table 1.*

Table 1. Positions and Sizes of the Openings (mm)

Opening no.	*x*	*d* / *s*	*g*
U (all thicknesses)			
1	97.5	22 / 19.5	13.0 / 15.5
2	132.5	22 / 19.5	13.0 / 15.5
3	167.5	22 / 19.5	13.0 / 15.5
4	202.5	22 / 19.5	73.0 / 75.5
G (t = 6, 7 mm)			
1	108.0	26 / 23.0	10.0 / 12.7
2	142.0	22 / 19.5	10.0 / 12.3
3	172.0	18 / 16.0	10.0 / 11.8
4	198.0	14 / 12.4	90.0 / 91.6
G (t = 8 mm)			
1	108.0	24 / 21.3	10.0 / 12.6
2	141.0	22 / 19.5	10.0 / 12.3
3	171.0	18 / 16.0	10.0 / 11.8
4	197.0	14 / 12.4	92.0 / 93.6

U: uniform and G: graded layout; *x*: opening-centre coordinate measured from the beam end (the other half is mirrored about midspan); *d*: diameter of the circular opening; *s*: side of the square opening before corner rounding; *g*: clear distance to the next opening (circle / square).

2.2 Material Model and Solution Settings

All calculations were performed in ANSYS 2020 R1 (Mechanical APDL) on a Dell Precision 7820 Tower workstation with two Intel Xeon Silver 4114 processors (2.20 GHz, 20 cores, 40 logical processors), 31.6 GB RAM and an NVIDIA Quadro P2000 graphics card (4 GB). The profile material is S355 with E = 210 GPa and ν = 0.30 and a multilinear isotropic hardening law (18 points, initial yield stress 355 MPa) taken from Table 2 of [18]; the same law is used for all sections, so that differences arise from geometry. Plates are linear elastic, rollers are rigid, plates are bonded to the profile, and the friction coefficient at the roller–plate and roller–profile contacts is 0.15. The loading roller is displaced downwards by 10 mm in 20 increments of 0.5 mm with large deformations enabled. The force is the vertical reaction of the loading roller and the displacement is the imposed roller displacement.

2.3 Finite Element Mesh

The profile and plates are meshed with 20-node SOLID186 hexahedral elements generated by an in-house Python mesher, with structured blocks on the flat walls, the corner arcs and around each opening (Fig. 3). The baseline mesh (L1) has two elements through the thickness, eight along a flat wall segment and three on each corner arc, and 8,536 elements in the beam for R6 and up to 10,488 for the graded variants. The maximum equiangular skewness is 0.167 for R6 and 0.348 for the perforated models (limit 0.4).

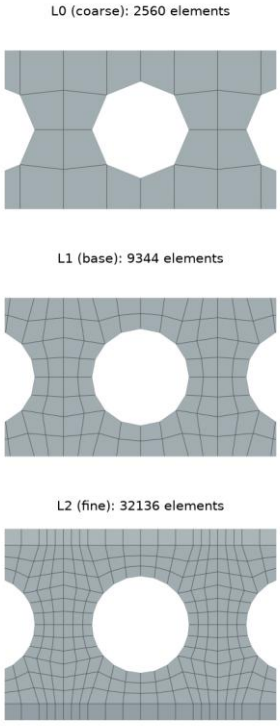


Fig. 3. *mesh around an opening of P6_C_U at three levels (L0 coarse, L1 base, L2 fine).*

2.4 Analytical Check of The Reference Section

The initial stiffness of R6 was compared with classical beam theory. The section properties, with the rounded corners, are A = 1203 mm², I = 561 × 10³ mm⁴, W_{el} = 18.7 × 10³ mm³ and W_{pl} = 23.7 × 10³ mm³; the area corresponds to a profile mass of 4.723 kg, identical to the mass of the CAD solid. The shear area is approximated by Eq. (1), giving A_v = 648 mm², and the stiffness of the simply supported beam under a midspan load, including bending and shear deformations, is given by Eq. (2).

$$A_v = 2\,t\,(B - t) \tag{1}$$

$$k = [\, L^3 / (48\, E\, I) + L / (4\, G\, A_v) \,]^{-1} \quad (2)$$

Equation (2) gives 66.2 kN/mm (76.3 kN/mm for bending only). The finite element stiffness related to the roller displacement, 52.0 kN/mm, is 21 % lower. The mid-span deflection of the bottom wall, however, was 0.383 mm at the force of 25.98 kN of the first load step, a stiffness of 67.8 kN/mm, which is 2.4 % above the beam-theory value; the remaining 0.117 mm (23 %) of the roller displacement arises from the local indentation of the thin walls under the roller and from the contact compliance, which the beam model does not contain. With the nominal yield stress f_y = 355 MPa (no safety or partial factors are applied) and L = 420 mm, the first-yield force and the plastic limit force of the beam model follow from Eqs. (3) and (4):

$$F_y = 4\, W_{el} f_y / L \quad (3)$$

$$F_{pl} = 4\, W_{pl} f_y / L \quad (4)$$

They are 63.2 kN and 80.1 kN. The finite element force is 62.4 kN at 2 mm, 77.2 kN at 8 mm and 79.2 kN at 10 mm, i.e. 3.6 % and 1.1 % below the plastic limit force at 8 and 10 mm; at the first-yield force the mid-span deflection (1.12 mm at 62.4 kN) is 17 % larger than the beam-theory value of 0.96 mm, because yielding beneath the roller starts earlier (Section 3.1). The comparison is a physical plausibility check, not a validation.

2.5 Mesh Convergence

Three levels (L0 coarse, L1 baseline, L2 fine; 2,400–2,944, 8,536–10,488 and 29,784–35,808 elements) were solved to 8 mm displacement for R6, the 6 mm uniformly circular-perforated P6_C_U and the 8 mm graded circular-perforated P8_C_G; the element size is reduced by a factor of about 1.5 between the levels. The initial stiffness k_0 (Eq. (5)) and the forces at 2, 4 and 8 mm were compared (Table 2).

$$k_0 = F(0.5\ \text{mm}) / (0.5\ \text{mm}) \quad (5)$$

Table 2. Convergence of the Mesh Study

Model	Level	k_0	F at 2 mm	F at 4 mm	F at 8 mm
R6	L0	51.36	63.38	70.18	76.13
R6	L1	51.96	62.43	71.69	77.20
R6	L2	51.85	62.08	71.56	77.28
P6_C_U	L0	46.42	61.80	69.15	74.63
P6_C_U	L1	47.16	60.14	70.44	75.99
P6_C_U	L2	46.99	60.11	70.19	75.74
P8_C_G	L0	57.53	82.96	93.01	101.00
P8_C_G	L1	59.53	81.74	93.77	102.22
P8_C_G	L2	59.19	80.82	93.53	101.51

k_0 in kN/mm; forces in kN.

The largest difference between L1 and L2 is 1.14 % (force at 2 mm in P8_C_G); for R6 and P6_C_U it is at most 0.56 %, and L0 differs from L1 by 0.8–3.4 %. Convergence is not monotonic for eight of the twelve quantities. The Richardson error estimate after Roache [19], Eq. (6), applied without a safety factor, was therefore evaluated only for monotonic cases; it is 0.34 % for the force at 2 mm in R6 and 4.1 % for the force at 2 mm in P8_C_G, which indicates that the direct L1–L2 difference (1.1 %) may underestimate the discretization error. The response ratios between the perforated sections and R6 change by at most 0.011 between L1 and L2. In Eq. (6), E is the estimated relative error of the fine-mesh result, $\varepsilon = (f_2 - f_1) / f_1$ the relative difference between the medium (f_2) and fine (f_1) mesh results, r = 1.5 the refinement ratio and p the observed order of convergence.

$$E = |\varepsilon| / (\, r^p - 1\,) \quad (6)$$

3. RESULTS

3.1 Force–Displacement Response

Figure 4a shows the force–displacement curves and Table 3 the characteristic measures. The force increases almost linearly up to about 0.5 mm, then the slope decreases as plastic zones develop under the loading roller, and the force continues to rise because of hardening and the change of geometry. The energy is the area under the curve from 0 to 10 mm, Eq. (7), i.e. the work done by the load roller (F in kN, u in mm, U in J); it is not impact or fracture energy.

$$U = \int_0^{10} F(u)\, \mathrm{d}u \quad (7)$$

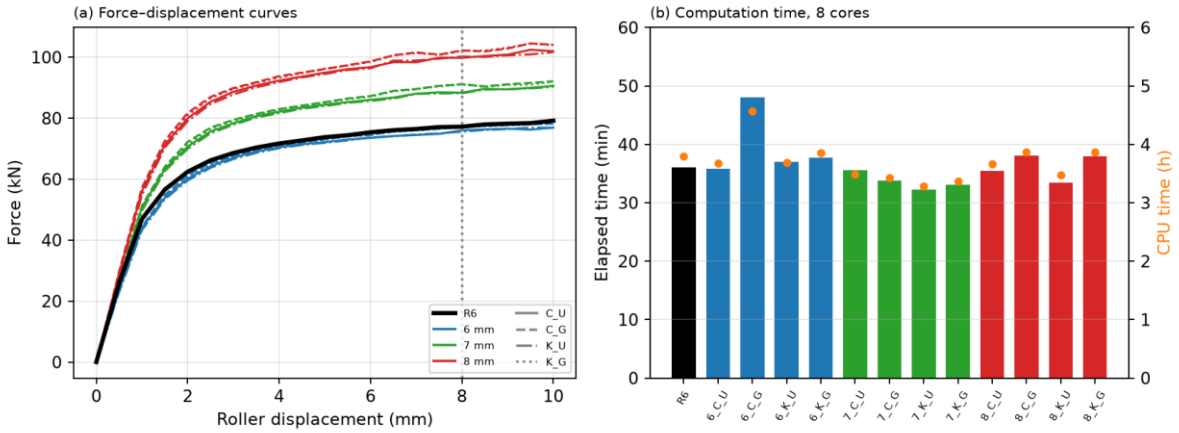


Fig. 4. *(a) force–displacement curves of the 13 models (black: solid reference R6; colour: wall thickness 6, 7 and 8 mm; line style: C_U solid, C_G dashed, K_U dash-dotted, K_G dotted); (b) elapsed time (bars) and CPU time (dots) of the calculations with eight cores.*

Table 3. Mass and Bending Response of the Profiles

Model	Mass (kg)	k_0 (kN/mm)	F at 8 mm (kN)	Energy 0–10 mm (J)
R6	4.723	52.0	77.2	673
P6_C_U	4.436	47.2	76.0	655
P6_C_G	4.474	47.7	77.0	665
P6_K_U	4.442	45.9	75.6	653
P6_K_G	4.480	46.5	77.1	662
P7_C_U	4.995	53.3	88.4	767
P7_C_G	5.039	53.9	91.1	779
P7_K_U	5.002	51.8	88.2	763
P7_K_G	5.046	52.4	91.1	776
P8_C_U	5.502	58.3	99.8	863
P8_C_G	5.573	59.5	102.2	879
P8_K_U	5.510	56.7	100.2	858
P8_K_G	5.580	58.1	102.1	876

ANSYS results on the L1 mesh. k_0 is the secant stiffness of the first 0.5 mm increment; first-yield loads are not compared, because the apparent first yielding of R6 near 36.9 kN is local yielding beneath the loading roller.

3.2 Effects of Openings and Wall Thickness

At t = 6 mm the perforated sections are 5.1–6.1 % lighter than R6 (4.436–4.480 kg against 4.723 kg), and their initial stiffness is 8.2–11.6 % lower (45.9–47.7 against 52.0 kN/mm). Their force at 8 mm is 75.6–77.1 kN, only 0.2–2.1 % below the R6 force of 77.2 kN, and the energy to 10 mm is 1.2–3.0 % lower. At 7 mm the perforated sections are 5.8–6.8 % heavier than R6, with an initial stiffness between 0.2 % below and 3.7 % above R6 and a force at 8 mm 14.2–18.1 % higher; at 8 mm they are 16.5–18.2 % heavier, with 9.2–14.6 % higher stiffness and 29.3–32.4 % higher force. Circular openings give 2.4–2.8 % higher initial stiffness than square ones, and the graded layout gives 1.3–3.3 % higher force at 8 mm than the uniform layout (in the 8 mm graded models the largest opening is 24 instead of 26 mm, so that the effect cannot be attributed to the arrangement alone).

3.3 Equivalent Wall Thickness

For each shape and layout, the thickness at which a criterion equals the R6 value was found by piecewise linear interpolation of the response between the 6, 7 and 8 mm results, Eq. (8) (Y: value of the criterion at thickness t_i; Y_{R6}: its value for R6), and the mass change relative to R6 follows from Eq. (9) (positive: lighter). All values lie within 6–8 mm; no extrapolation was needed (Table 4).

$$t_{eq} = t_i + (Y_{R6} - Y_i)\,(t_{i+1} - t_i) / (Y_{i+1} - Y_i) \quad (8)$$

$$\Delta m = [\, m_{R6} - m(t_{eq}) \,] / m_{R6} \times 100\ \% \quad (9)$$

Table 4. Wall Thickness Giving The R6 Value and Mass Change

Criterion	Variant	t_{eq} (mm)	Δm (%)
k_0	C_U	6.79	-3.2
k_0	C_G	6.69	-3.0
k_0	K_U	7.03	-6.2
k_0	K_G	6.92	-5.9
F at 8 mm	C_U	6.10	+4.9
F at 8 mm	C_G	6.01	+5.1
F at 8 mm	K_U	6.13	+4.4
F at 8 mm	K_G	6.01	+5.0
Energy	C_U	6.16	+4.1
Energy	C_G	6.07	+4.4
Energy	K_U	6.19	+3.7
Energy	K_G	6.09	+4.0

Δm positive = lighter than R6; energy = 0–10 mm.

To keep the initial stiffness of R6, the perforated walls must be thickened to 6.69–7.03 mm and are then 3.0–6.2 % heavier than R6, so that perforation gives no mass saving. To keep the force at 8 mm, 6.01–6.13 mm suffice and the sections are 4.4–5.1 % lighter; for the energy to 10 mm the thickness is 6.07–6.19 mm and the saving 3.7–4.4 %. The force at 8 mm per unit mass of the perforated 6 mm sections is 17.0–17.2 kN/kg against 16.3 kN/kg for R6, whereas the initial stiffness per unit mass is lower, 10.3–10.7 against 11.0 kN/(mm·kg). A linear interpolation between the 6 and 8 mm results alone predicts the 7 mm values within 1.7 % and changes the equivalent thicknesses by at most 0.09 mm. Repeating the interpolation for force values at 2, 4, 6, 8 and 10 mm (Table 5) gives force-equivalent thicknesses of 6.01–6.27 mm and mass savings of 2.7–3.9 % at 2 mm and 3.9–5.1 % at 4–10 mm; for the work done the savings are 0.3–1.9 % up to 2 mm and 2.6–4.4 % up to 4 mm or more. The sign of the result is therefore the same at every level, but its magnitude is smallest in the early plastic range. Figure 6 shows the relation between profile mass and the three response measures for all 13 models.

Table 5. Sensitivity of the Equivalent Thickness to the Displacement

Criterion	t_{eq} (mm)	Δm (%)
Force at 2 mm	6.11–6.27	+2.7 to +3.9
Force at 4 mm	6.05–6.13	+4.3 to +4.8
Force at 6 mm	6.07–6.15	+4.3 to +4.5
Force at 8 mm	6.01–6.13	+4.4 to +5.1
Force at 10 mm	6.07–6.17	+3.9 to +4.4
Energy 0–2 mm	6.28–6.47	+0.3 to +1.9
Energy 0–4 mm	6.15–6.29	+2.6 to +3.5
Energy 0–6 mm	6.11–6.22	+3.3 to +4.0
Energy 0–8 mm	6.09–6.20	+3.6 to +4.2
Energy 0–10 mm	6.07–6.19	+3.7 to +4.4

Range over the four variants (C_U, C_G, K_U, K_G); Δm as in Table 4.

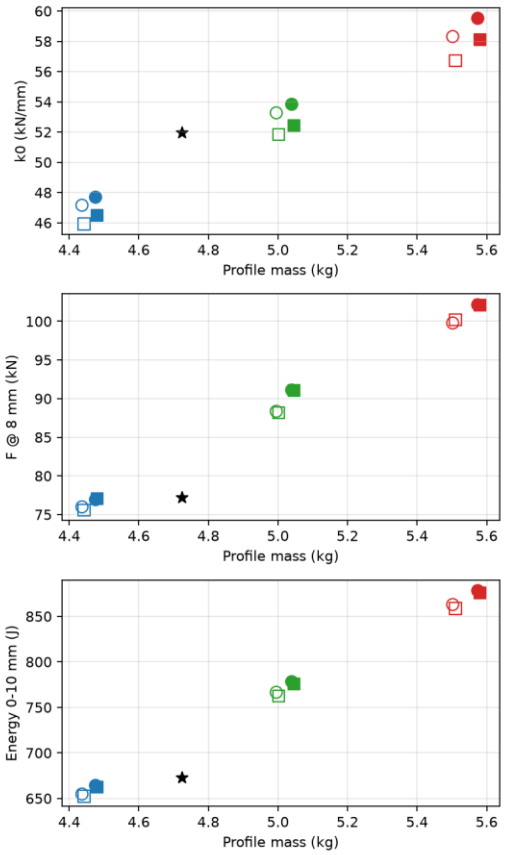


Fig. 6. *profile mass versus k_0, force at 8 mm and energy for the 13 models (colour: wall thickness 6, 7, 8 mm; circles: circular, squares: square openings; filled: graded, open: uniform layout; star: R6).*

3.4 Stress and Strain

Figure 5 shows the equivalent (von Mises) stress and the equivalent plastic strain of R6 and P6_C_U at 10 mm roller displacement (displacements magnified twice). In both models the plastic strain is concentrated under the loading roller, on the top wall and the adjacent side walls; around the openings of P6_C_U it is low compared with the region under the roller, although stress concentrations appear at the edges of the openings. The values are nodal values at corner nodes, and ANSYS reported distorted elements at the contact line under the roller; pointwise maxima are therefore not used as measures of local strain.

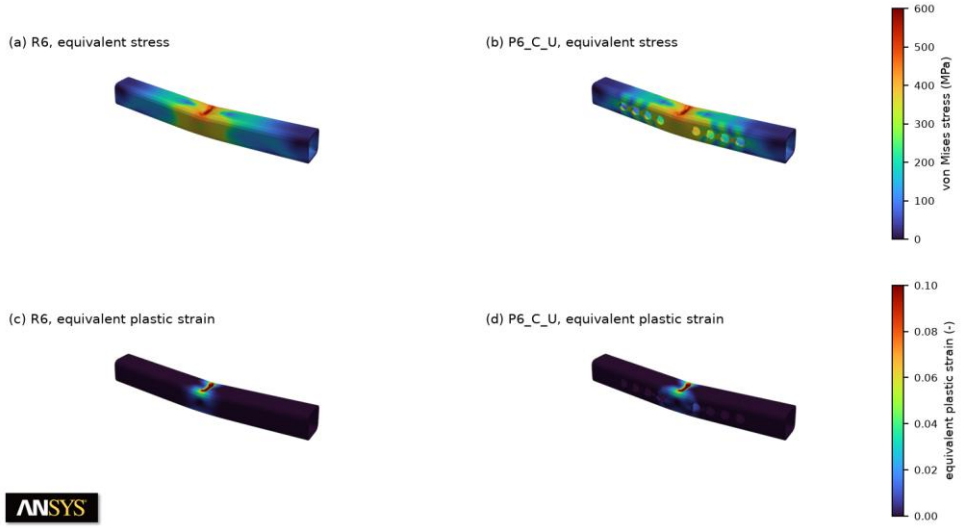


Fig. 5. *equivalent stress (a, b) and equivalent plastic strain (c, d) of R6 and P6_C_U at 10 mm roller displacement (displacements magnified twice; nodal values at corner nodes).*

3.5 Computational Time

With eight cores (Fig. 4b), one model took 32–48 min of elapsed time (CPU time 3.3–4.6 h) up to 10 mm displacement, and the fine meshes of the mesh study (about 35,000–42,000 elements, 16 steps to 8 mm) took 110–130 min (CPU time 11.4–12.7 h). The P8 and P6_K_G calculations were repeated with eight cores so that all runs have the same conditions, and the repeated runs reproduced the forces at 0.5 and 8 mm of the first runs to six digits. The CPU time is the sum over all threads, and some runs were carried out at the same time as other calculations on the same machine.

4. DISCUSSION

The perforated 6 mm sections are 5.1–6.1 % lighter than R6, but their initial stiffness falls by 8.2–11.6 %, about twice as much as the mass, whereas the force at 8 mm and the energy to 10 mm are almost unchanged (−2.1 to −0.2 % and −3.0 to −1.2 %). Statements that a perforated section is more efficient are therefore meaningful only when the performance objective is specified: retaining the stiffness of R6 requires 6.7–7.0 mm walls and removes the mass advantage, while the force at 8 mm is matched at 6.0–6.1 mm with 4–5 % less mass. The quasi-static force at 8 mm is not a measure of ultimate strength, fatigue resistance, buckling capacity or impact performance.

The small change of the force at large displacement can be explained by the position of the openings. The plastic deformation concentrates under the loading roller, in the intact zone from 220 to 280 mm (Fig. 5), where the bending moment is at its maximum. The opening of the uniform layout nearest to the load is centred 47.5 mm from the centre of the beam (x = 202.5 mm, supports at x_s = 40 and 460 mm), where the bending moment is 77 % of the maximum (Eq. (10)). Removing a 22 mm high part of both side walls at this section reduces the

plastic section modulus by 1452 mm³, i.e. by 6.1 % of 23 675 mm³ (Eq. (11)); the section keeps 94 % of its plastic moment capacity while carrying 77 % of the maximum moment, a utilisation of 82 % (Eq. (12)); in the graded layout, with a 14 mm opening nearest to the load, it is 77 %.

$$M(x) / M_{max} = (x - x_s) / (L / 2) \quad (10)$$

$$\Delta W_{pl} = t\, d^2 / 2 \quad (11)$$

$$\eta = [\, M(x) / M_{max} \,] / [\, 1 - \Delta W_{pl} / W_{pl} \,] \quad (12)$$

In this loading arrangement the openings therefore lower the stiffness, consistent with additional shear and Vierendeel deformation in the perforated zones, whereas the plastic limit force estimated for the beam model is governed by the intact section under the roller and is not expected to be reduced by them; the forces of the perforated 6 mm profiles at 8 mm are 0.2–2.1 % lower than that of R6. Openings in the zone of the maximum moment would be expected to reduce the limit force by about the loss of plastic section modulus at that section (6–9 % for openings of 22–26 mm in 6 mm walls). The finite element solution of the reference profile agrees with the analytical solution of the beam: the stiffness of the mid-span deflection is 2.4 % above the beam-theory value, and the forces at 8 and 10 mm are 3.6 % and 1.1 % below the plastic limit force (Section 2.4); the 21 % lower stiffness related to the roller displacement is the local indentation beneath the roller. The mesh study gives a discretization error of about 4.1 % for one force of the P8_C_G model and at most 1.1 % elsewhere in the L1–L2 comparison, and the ratios to R6 change by less than 0.011.

Studies of perforated beams report the effect of openings on capacity or buckling [1–6, 8–12]; the tests and finite element study of Ridley-Ellis et al. [15] are the closest in loading and openings, and Rajana et al. described the stiffness of perforated cellular beams through the variation of the cross-section inertia [20]. The present comparison differs in that the wall thickness is the variable and the section is re-sized until it matches the solid reference. The approach follows the strength-based finite element analyses of machine structures by Çelik et al., of a tillage tool [21], a rotary drum mower [22] and an engine mounting bracket [23]; in [22] the calculated and measured stresses differed by 24.25 % on average, so that absolute values of such models can deviate from measurements, whereas comparisons between sections that share material data, meshing rules and boundary conditions are less affected. The material model is an input of the same kind, as the review of Çelik et al. on assigned material properties notes [24].

Whether the openings are worth making depends on what the member must do. Where deflection must be kept small, the solid 6 mm profile is the better choice: the perforated profiles are 5.1–6.1 % lighter but 8.2–11.6 % less stiff, their stiffness per unit mass is 3–6 % lower, and restoring the stiffness requires a non-standard 6.7–7.0 mm wall or the standard 8 mm wall, which is 16.5–18.2 % heavier than R6. Where the force carried at a large deflection matters most, the perforated 6 mm profile is the better choice: it carries 97.9–99.9 % of the R6 force at 8 mm with 5.1–6.1 % less mass, and the equivalent thickness of 6.0–6.1 mm is practically the standard 6 mm wall. Cases of the first kind may include frames and guides of machine tools and measuring equipment and beams with a deflection limit; cases of the second kind may include machine frames, supports and guards that must carry a given load after they have deformed. The saving of about 4–5 % is moderate and has to be weighed against the additional operation of making 16 openings per profile, the stress concentrations at their edges and the loss of the closed wall as a seal. In series production the openings may therefore be worthwhile for members of the second kind, if the cost of the additional operation is smaller than the value of a 4–5 % mass saving, whereas for members of the first kind the solid profile appears preferable.

5. CONCLUSIONS

1. At a wall thickness of 6 mm, 16 side-wall openings reduce the profile mass of a 60 × 60 mm S355 hollow section by 5.1–6.1 %.
2. The initial stiffness is 8.2–11.6 % lower, whereas the force at 8 mm displacement is only 0.2–2.1 % lower than that of the solid-wall reference.
3. The equivalent wall thicknesses, interpolated from the 6, 7 and 8 mm results, are 6.0–6.1 mm for force at 8 mm (4.4–5.1 % lower mass), 6.1–6.2 mm for energy up to 10 mm (3.7–4.4 % lower mass) and 6.7–7.0 mm for initial stiffness (3.0–6.2 % higher mass). Perforation saves 4–5 % of mass if force or energy at large displacement governs, but adds 3–6 % if stiffness governs.
4. The effects of the opening shape and arrangement are below about 3 %, larger than the discretization differences of the three mesh-studied models (at most 1.1 %) but small.
5. Mesh refinement by a factor of about 1.5 changed the initial stiffness and the forces by at most 0.6 % for R6 and P6_C_U and 1.1 % for P8_C_G, and the ratios to R6 by at most 0.011.
6. The finite element solution of the reference profile agrees with beam theory: 2.4 % in the mid-span deflection stiffness and 1.1–3.6 % below the plastic limit force at 10 and 8 mm.
7. With eight cores, one model took 32–48 min up to 10 mm displacement (CPU time 3.3–4.6 h).
8. Where deflection must be kept small, the solid 6 mm profile is preferable; where the force carried at large deflection matters most and a mass saving of 5–6 % justifies the cost of making the openings, the perforated 6 mm profile may be used.

DECLARATION OF GENERATIVE AI USE

Generative AI tools were used for the page layout and the editing of this manuscript.

REFERENCES

[1] K. D. Tsavdaridis and C. D'Mello, "Web buckling study of the behaviour and strength of perforated steel beams with different novel web opening shapes," *Journal of Constructional Steel Research*, vol. 67, no. 10, pp. 1605–1620, 2011, doi:10.1016/j.jcsr.2011.04.004.

[2] E. Ellobody, "Interaction of buckling modes in castellated steel beams," *Journal of Constructional Steel Research*, vol. 67, no. 5, pp. 814–825, 2011, doi:10.1016/j.jcsr.2010.12.012.

[3] A. M. I. Sweedan and K. M. El-Sawy, "Elastic local buckling of perforated webs of steel cellular beam–column elements," *Journal of Constructional Steel Research*, vol. 67, no. 7, pp. 1115–1127, 2011, doi:10.1016/j.jcsr.2011.02.004.

[4] D. Sonck and J. Belis, "Lateral–torsional buckling resistance of cellular beams," *Journal of Constructional Steel Research*, vol. 105, pp. 119–128, 2015, doi:10.1016/j.jcsr.2014.11.003.

[5] N. E. Shanmugam, V. T. Lian and V. Thevendran, "Finite element modelling of plate girders with web openings," *Thin-Walled Structures*, vol. 40, no. 5, pp. 443–464, 2002, doi:10.1016/S0263-8231(02)00008-3.

[6] C. Vadivelu, V. Prabaharan and P. K. Akhas, "Flexural behavior of perforated rectangular hollow section cold-formed steel beams: An experimental and numerical study," *Results in Engineering*, vol. 26, art. 104821, 2025, doi:10.1016/j.rineng.2025.104821.

[7] S. I. Cosgun and M. E. Akcan, "Experimental and numerical study on eccentrically compression-loaded cold-formed flat oval-perforated steel square hollow-section stub columns," *Structures*, vol. 73, art. 108316, 2025, doi:10.1016/j.istruc.2025.108316.

[8] Z. Chen, Y. Huang and B. Young, "Design of cold-formed ferritic stainless steel RHS perforated beams," *Engineering Structures*, vol. 250, art. 113372, 2022, doi:10.1016/j.engstruct.2021.113372.

[9] A. Prabowo, Y. Huang and B. Young, "Cold-formed stainless steel beams with single web hole at elevated temperatures," *Thin-Walled Structures*, vol. 195, art. 111321, 2024, doi:10.1016/j.tws.2023.111321.

[10] A. Prabowo, "Flexural strength of RHS perforated lean duplex stainless steel beam at temperature 24–900 °C," *Civil Engineering*

Dimension, vol. 26, no. 1, pp. 71–80, 2024, doi:10.9744/ced.26.1.71-80.

[11] A. Saoula, M. M. Selim, S. A. Meftah, A. B. Benyamina and A. Tounsi, "Simplified analytical method for lateral torsional buckling assessment of RHS beams with web openings," *Structures*, vol. 34, pp. 2848–2860, 2021, doi:10.1016/j.istruc.2021.09.034.

[12] J. Lifsey, M. Sifan, K. Pologanathan, D. T. Gray, T. Kajaharan, K. Elilarasi and C. Higgins, "Flexural behaviour and design of modular construction optimised CFS beams with circular web openings," *Case Studies in Construction Materials*, vol. 23, art. e05220, 2025, doi:10.1016/j.cscm.2025.e05220.

[13] H. K. Çelik, A. E. W. Rennie and İ. Akıncı, "Design and structural optimisation of a tractor mounted telescopic boom crane," *Journal of the Brazilian Society of Mechanical Sciences and Engineering*, vol. 39, no. 3, pp. 909–924, 2017, doi:10.1007/s40430-016-0558-y.

[14] H. K. Çelik and İ. Akıncı, "Analytical and finite element method based stress analysis of rotary elements: case study for the motion transmission gears of a rotary drum mower," *Journal of Failure Analysis and Prevention*, vol. 16, no. 2, pp. 293–301, 2016, doi:10.1007/s11668-016-0084-3.

[15] D. J. Ridley-Ellis, J. S. Owen and G. Davies, "Flexural behaviour of rectangular hollow sections with circular side wall openings," in *Tubular Structures IX, Proc. 9th Int. Symp. and Euroconference*, Düsseldorf, Germany, 3–5 April 2001, pp. 339–348.

[16] M. A. Dundar and M. Nuraliyev, "Parametric study on the assessment of the local buckling behavior of perforated square hollow sections with non-uniform wall thickness under axial compression," *Journal of Innovative Engineering and Natural Science*, vol. 4, no. 2, pp. 326–353, 2024, doi:10.61112/jiens.1397391.

[17] T. Gajewski, N. Staszak and T. Garbowski, "Parametric optimization of thin-walled 3D beams with perforation based on homogenization and soft computing," *Materials*, vol. 15, no. 7, art. 2520, 2022, doi:10.3390/ma15072520.

[18] G. İrsel, "Bend radius (R/t) effects on stress in S355 sheet bending: elastic vs. elastoplastic finite element analysis," *Journal of the Technical University of Gabrovo*, vol. 72, no. 1, pp. 3–8, 2026, doi:10.62853/ORIL6756.

[19] P. J. Roache, "Perspective: A method for uniform reporting of grid refinement studies," *Journal of Fluids Engineering*, vol. 116, no. 3, pp. 405–413, 1994, doi:10.1115/1.2910291.

[20] K. Rajana, A. Alonso-Rodríguez and K. D. Tsavdaridis, "A wavelet-based approach for describing the mechanical behaviour of cellular beams," *Steel Construction*, vol. 14, no. 1, pp. 47–54, 2021, doi:10.1002/stco.202000043.

[21] H. K. Celik, N. Caglayan, M. Topakci, A. E. W. Rennie and I. Akinci, "Strength-based design analysis of a Para-Plow tillage tool," *Computers and Electronics in Agriculture*, vol. 169, art. 105168, 2020, doi:10.1016/j.compag.2019.105168.

[22] H. K. Celik, I. Akinci, N. Caglayan and A. E. W. Rennie, "Structural strength analysis of a rotary drum mower in transportation position," *Applied Sciences*, vol. 13, no. 20, art. 11338, 2023, doi:10.3390/app132011338.

[23] H. K. Celik, H. Ersoy, A. Dogan, G. Eravci, A. E. W. Rennie and I. Akinci, "Strength-based design analysis of a damaged engine mounting bracket designed for a commercial electric vehicle," *Journal of Failure Analysis and Prevention*, vol. 21, no. 4, pp. 1315–1322, 2021, doi:10.1007/s11668-021-01177-9.

[24] H. K. Celik, S. Koc, A. Kustarci and A. E. W. Rennie, "A literature review on the linear elastic material properties assigned in finite element analyses in dental research," *Materials Today Communications*, vol. 30, art. 103087, 2022, doi:10.1016/j.mtcomm.2021.103087.